Compact Below-Cutoff Substrate Integrated Waveguide Bandpass Filters Based on Space-Filling I–H Slot Resonators

Rand Muaffaq Hadi

[1]Communication Engineering Department, Najaf Polytechnic College, Al-Furat Al-Awsat Technical University, Al-Najaf 31001, Iraq
Rand.muaffaq@atu.edu.iq

***Abstract*—Operating a substrate integrated waveguide (SIW) only above the cutoff of its dominant mode leads to bulky filters in the low-gigahertz range. In this work, a space-filling I–H slot is etched on the upper wall of an SIW so that transmission is obtained inside the evanescent band of the guide. The slot acts as a magnetic-dipole resonator; together with the negative effective permittivity of the guide below cutoff, it creates a backward-wave band followed directly by a forward-wave band. Slots of first, second and third order are compared inside an identical footprint, the effective permittivity and permeability are extracted from the simulated scattering parameters, and a lumped-element model with analytical expressions for the lower transmission zero and both resonant modes is fitted to the full-wave response. For the third-order slot on FR4 ($\varepsilon_r = 4.3$), the passband is located near 2.15 GHz, roughly 59% lower than the 5.2 GHz cutoff of the unloaded guide. A fabricated single-cell filter measures about 1.5 dB insertion loss including the SMA connectors, about 19 dB return loss, two transmission zeros and a board area of 17 × 17 mm² ($0.12\lambda_0 \times 0.12\lambda_0$). Cascaded two- and three-cell designs with steeper skirts are also reported and compared with recent SIW fractal and metamaterial filters.**

***Keywords*—SIW filter; below-cutoff propagation; space-filling slot; double-negative medium; lumped-element model; compact bandpass filter**

I. INTRODUCTION

The substrate integrated waveguide (SIW) transfers most of the merits of a metallic rectangular waveguide, namely low radiation, good power handling and a relatively high quality factor, to a planar printed circuit that can be integrated with microstrip and coplanar lines on the same board [1,2]. Its main drawback in the sub-6 GHz range is size: the width of the guide is fixed by the cutoff of the dominant TE_{10} mode, so a filter that operates above cutoff near 2 GHz occupies several square centimetres even on a high-permittivity laminate.

Many techniques have been proposed to shrink SIW components, as surveyed in [3]. Ridged SIW lowers the cutoff by loading the guide centre [4,5]; half-mode and quarter-mode SIW exploit the virtual magnetic wall of the TE_{10} field to remove one half or three quarters of the cavity [6–9]; folded SIW stacks the guide in two layers [10]; and slow-wave loadings increase the effective permittivity [11,12]. In all of these approaches, however, the passband still lies above the cutoff of the modified guide.

A different route is offered by metamaterial concepts [13,14]. A metallic waveguide below cutoff behaves as a medium with negative effective permittivity for the TE modes; if a resonant element that provides negative effective permeability is added, a backward-wave passband appears in the evanescent region [15]. In SIW technology, complementary split-ring resonators (CSRRs), derived from split rings by Babinet duality [16,17], have been etched on the broad wall to build very compact evanescent-mode filters [18–20], and CSRRs are also widely used to suppress spurious bands in planar filters [21]. Simple slots, which act as magnetic dipoles, yield negative-order resonances that were first exploited for miniaturized SIW antennas [22,23]. Stepped-impedance CSRRs further reduce the size of such unit cells [24].

Fractal curves are attractive in this context because their electrical length grows with every iteration while the occupied area remains constant [25,26]. Cross-shaped fractals on half-mode SIW [27], H-shaped fractal slots on SIW for C-band filters [28], Hilbert fractals [29] and hybrid fractal/CSRR/defected-ground loadings [30] have all produced strong size reduction. Most of these works, however, either concentrate on the C band or report the filter response without a circuit model that explains where the transmission zero and the two poles come from. A half-mode realisation of a slot-loaded cell of this kind has been described briefly in [31]; the present work concentrates on the full-mode structure and provides the order-by-order analysis, the extracted constitutive parameters and the circuit model.

The contributions of this paper are the following:

- an I–H fractal slot is studied over three iterations on a fixed footprint, and the resulting downward shift of the passband is quantified;
- the retrieved ε_{eff} and μ_{eff} and the surface-current distributions are used to identify the backward- and forward-wave regions below cutoff;
- an equivalent circuit is proposed whose closed-form resonances predict the lower transmission zero and the two passband poles, and it is validated against full-wave simulation;
- the effect of the slot size, the dispersion diagram, the dissipation and the phase response are analysed;
- one-, two- and three-stage filters are designed, and a one-stage prototype is fabricated and measured on low-cost FR4.

Section II describes the host SIW, Section III the fractal unit cells, Section IV the equivalent circuit, Section V the filters and the measurements, and Section VI the comparison with the literature. Conclusions are drawn in Section VII.

II. Host SIW Design

All structures are printed on FR4 with relative permittivity $\varepsilon_r = 4.3$, loss tangent $\tan\delta = 0.025$ and thickness $h = 1.5$ mm, with copper ($\sigma = 5.8 \times 10^7$ S/m) on both faces. All full-wave simulations and circuit optimisations were carried out with Keysight Advanced Design System (ADS), including dielectric and conductor losses.

For an SIW whose via rows are spaced W apart (centre to centre), with via diameter d and pitch p, the width of the equivalent rectangular waveguide is [1,2]

$$a_{\text{eff}} = W - \frac{d^2}{0.95\,p}, \qquad (1)$$

and the cutoff frequency of the TE $_{10}$ mode is

$$f_c = \frac{c_0}{2\,a_{\text{eff}}\sqrt{\varepsilon_r}}, \qquad (2)$$

where c_0 is the speed of light in vacuum. Leakage between the vias remains negligible when

$$p \le 2d \quad \text{and} \quad 0.05 < \frac{p}{\lambda_c} < 0.25, \qquad (3)$$

with $\lambda_c = 2a_{\text{eff}}$ the cutoff wavelength in the dielectric. With $W = 15$ mm, $d = 1$ mm and $p = 1.5$ mm, (1) gives $a_{\text{eff}} = 14.3$ mm and (2) gives $f_c \approx 5.06$ GHz; the full-wave simulation of the unloaded guide, which includes the feeding transitions, places the cutoff at about 5.2 GHz. Both via conditions in (3) are satisfied ($p/d = 1.5$ and $p/\lambda_c = 0.052$).

III. I–H Slot-Loaded Unit Cells

A. Fractal Geometry

A fractal curve is generated by replacing every segment of a starting shape with N scaled copies of itself, the scale factor being $s < 1$. Its similarity dimension is

$$D = \frac{\ln N}{\ln(1/s)}. \qquad (4)$$

A straight line has $D = 1$, whereas space-filling curves approach $D = 2$ and therefore pack a long conductor, or slot, into a small area [25]. Fig. 1 compares a straight slot with an I–H fractal slot of the same total length. The hybrid curve used here starts from an "I" shape (first iteration); in each further iteration, every free end is replaced by a smaller "H", so that the slot length grows rapidly while the bounding square of side b is kept unchanged.



Fig. 1. A straight slot and an I–H fractal slot of equal length.

B. Operating Principle

Below f_c the TE $_{10}$ field of the SIW decays exponentially, and the guide can be described by a negative effective permittivity. The vertical electric field of the mode is strongest along the guide centre, so a slot placed there is excited efficiently and behaves as a magnetic dipole oriented along the guide. Close to its resonance this dipole produces a negative effective permeability. In the frequency range where both quantities are negative, the medium is double negative (DNG) and supports a backward wave; immediately above it, both quantities become positive (DPS) and a forward wave propagates. The slot is etched on the top wall so that the ground plane remains solid, which keeps radiation and coupling to other circuits low.

Fig. 2 shows the unloaded SIW and the unit cells with the first, second and third fractal iterations. All cells have the same footprint, with fractal side $b = 12.5$ mm and slot width $g = 0.5$ mm.

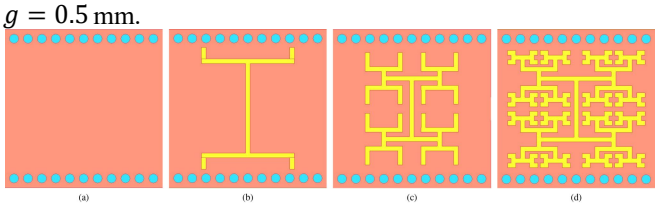
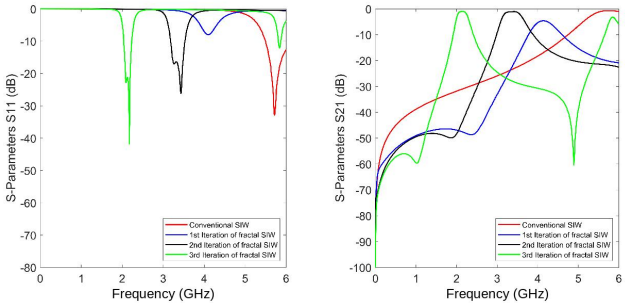


Fig. 2. Unit cells: (a) unloaded SIW; (b) first, (c) second and (d) third iteration of the I–H fractal slot.

C. Simulated Response of the Unit Cells

The simulated reflection and transmission coefficients of the four cells are plotted in Fig. 3. The unloaded SIW is a high-pass structure that starts to transmit at about 5.2 GHz. Each fractal cell introduces a passband below this frequency. The first iteration resonates near 4.1 GHz but is poorly matched ($|S_{21}| \approx -4.4$ dB). The second iteration is centred at about 3.4 GHz, and the third at about 2.15 GHz, both with a transmission close to 0 dB. The third-iteration cell shows two reflection minima, at about 2.08 and 2.17 GHz, which are the two coupled modes discussed in Section IV, and two transmission zeros, near 1 and 4.9 GHz, which sharpen both skirts.



(a) (b)

Fig. 3. Simulated (a) $|S_{11}|$ and (b) $|S_{21}|$ of the unloaded SIW and of the three fractal unit cells.

Because the cells share the same footprint, the downward shift of the passband is equivalent to a size reduction. It is quantified with respect to the cutoff of the unloaded SIW as

$$\eta_n = \frac{f_c - f_0^{(n)}}{f_c} \times 100\%, \qquad (5)$$

where $f_0^{(n)}$ is the centre frequency of the nth iteration. The results, collected in Table I, show that the third iteration places the passband about 59% below cutoff.

TABLE I. Centre frequency of the unit cells (common footprint).

Structure	f_0 (GHz)	η (%)
Unloaded SIW (cutoff)	5.2	–
1st iteration	4.1	21.2
2nd iteration	3.4	34.6
3rd iteration	2.15	58.7

The simulated surface-current distributions in Fig. 4 confirm this behaviour. At 2 GHz, the current in the unloaded SIW decays rapidly away from the input port, as expected for an evanescent mode, whereas in the third-

iteration cell it is concentrated along the fractal slot and reaches the output port. At 1 GHz (lower transmission zero) and at 5 GHz (upper stopband) the current in the fractal cell remains confined near the input.

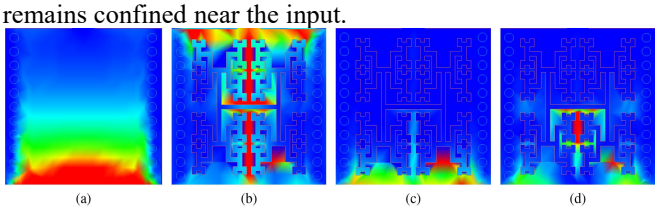


Fig. 4. Simulated surface current: (a) unloaded SIW at 2 GHz; third-iteration cell at (b) 2 GHz, (c) 1 GHz and (d) 5 GHz.

D. Retrieved Constitutive Parameters

The effective permittivity and permeability of the third-iteration cell were retrieved from its simulated S-parameters by the standard inversion procedure of [32]. As shown in Fig. 5, both real parts are negative between 1.97 and 2.17 GHz, which is the backward-wave (DNG) band, and both are positive between 2.17 and 2.42 GHz, which is the forward-wave (DPS) band. The two bands are adjacent and together form the passband of the cell, which explains its dual-mode response. The dispersion diagram in Fig. 6 confirms this interpretation: the normalised phase constant has a negative slope in the first band and a positive slope in the second, and the attenuation constant drops to almost zero across both bands without any gap at the transition, so the backward and forward bands merge into a single balanced passband.

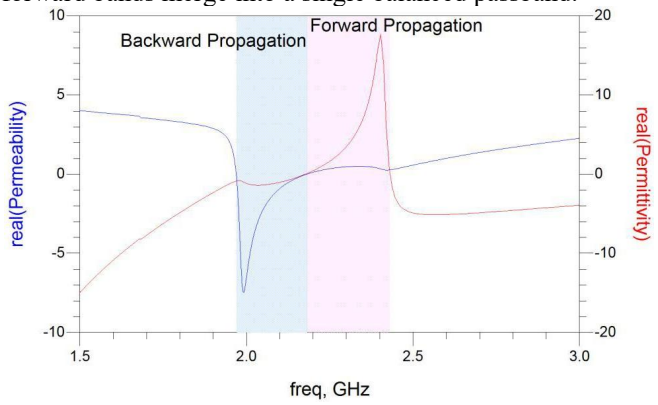


Fig. 5. Real parts of the retrieved permeability and permittivity of the third-iteration cell, with the backward- and forward-wave bands shaded.

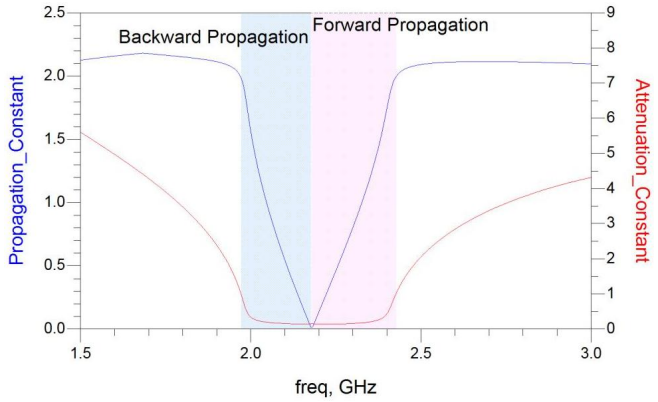


Fig. 6. Normalised phase constant and attenuation constant of the third-iteration cell.

E. Effect of the Slot Size

Fig. 7(a) compares the transmission of the third-iteration cell with that of an unloaded SIW of the same size, and Fig. 7(b) shows the effect of the fractal side length b. Reducing b from 12.5 mm to 10 mm and 8 mm shortens the slot and moves the passband upward, so b is the primary parameter for setting the centre frequency. The largest value, $b = 12.5$ mm, was retained for all the filters.

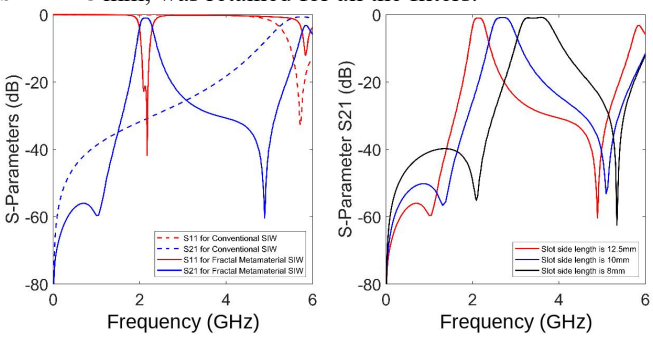


Fig. 7. (a) Third-iteration cell compared with an unloaded SIW of the same size; (b) $|S_{21}|$ of the third-iteration cell for $b = 12.5$, 10 and 8 mm.

IV. Equivalent-Circuit Model

The circuit of Fig. 8 describes the third-iteration cell. The SIW is treated as a two-wire line formed by its top and bottom walls, with series inductance L_d and shunt capacitance C_d. Each via row is a set of short-circuited stubs that appears, seen from the guide centre, as a shunt inductance L_{via}; this inductance is responsible for the high-pass behaviour of the unloaded SIW. The fractal slot is represented by a series capacitance C_{frac}. Its coupling to the guide is partly magnetic, modelled by the inductance L_c in parallel with C_{frac}, and partly electric, modelled by the shunt capacitance C_c between the ground plane and the small patches enclosed by the slot arms.

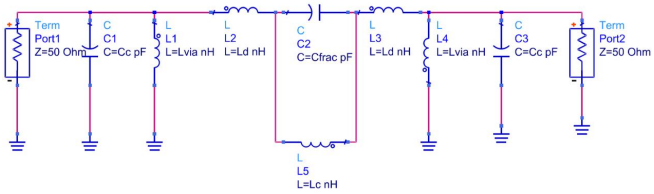


Fig. 8. Equivalent circuit of the third-iteration SIW–fractal unit cell.

The parallel L_c–C_{frac} branch lies in the signal path; at its resonance it behaves as an open circuit, which produces the transmission zero below the passband:

$$f_z = \frac{1}{2\pi\sqrt{L_c\, C_{\text{frac}}}}. \qquad (6)$$

Increasing L_c, i.e., strengthening the magnetic coupling through a wider slot or a different slot position, moves the zero downward and sharpens the lower skirt. The frequencies of the two modes are approximately

$$f_1 = \frac{1}{2\pi\sqrt{(L_d + L_{\text{via}})(C_{\text{frac}} + C_d + C_c)}}, \qquad (7)$$

$$f_2 = \frac{1}{2\pi\sqrt{L_{\text{via}}(C_d + C_c)}}, \qquad (8)$$

Once the host SIW is fixed, L_d, C_d and L_{via} hardly change, so C_{frac} and C_c, which depend on the slot size, width and position and on the substrate permittivity, are the main tuning parameters; C_{frac} affects both f_z and f_1.

The values $L_c = 10.52$ nH, $C_{\text{frac}} = 2.11$ pF, $L_{\text{via}} = 0.364$ nH, $C_d = 8.96$ pF and $L_d \approx 10^{-6}$ nH were obtained with the optimiser of ADS by fitting the circuit

response to the full-wave S-parameters, and the coupling capacitance was then set to $C_c = 5.0$ pF so that the two poles of the model coincide with the reflection minima of the full-wave response. The very small L_d shows that the series inductance of the short SIW section is negligible. With these values, (6) gives $f_z = 1.07$ GHz, and (7)–(8) give $f_1 \approx 2.08$ GHz and $f_2 \approx 2.23$ GHz, close to the simulated zero near 1.1 GHz and to the two reflection minima of the cell.

Fig. 9 compares the circuit and full-wave responses. The agreement is good across the passband and the lower stopband. The upper zero near 4.9 GHz is not reproduced, because the lumped model neglects the higher-order resonances of the slot, as well as the dielectric, conductor and radiation losses. Despite its simplicity, the model identifies which physical dimension controls each feature of the response.

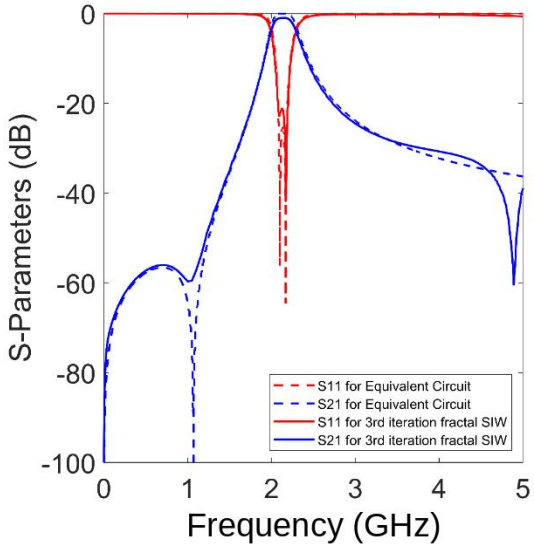


Fig. 9. Full-wave and equivalent-circuit S-parameters of the third-iteration cell.

The dissipated power fraction,

$$L_{\text{diss}} = 1 - |S_{11}|^2 - |S_{21}|^2, \qquad (9)$$

is plotted in Fig. 10. It peaks at about 0.16 inside the passband, where the fields are strongest, and is dominated by the dielectric loss of FR4. Radiation from the slot grows with the slot width; it remains small for $g = 0.5$ mm and can be suppressed further by a shielding cover without affecting neighbouring circuits.

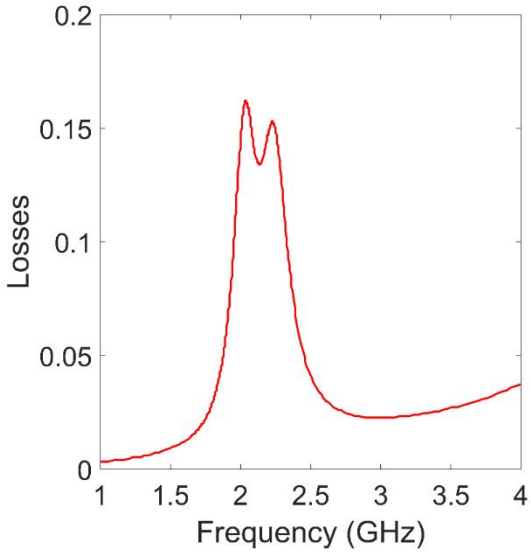


Fig. 10. Dissipated power fraction of the third-iteration cell.

V. Filter Design, Fabrication and Measurement

A. One-Stage Filter

The third-iteration cell is fed by $50\,\Omega$ microstrip lines through tapered transitions, as shown in Fig. 11; the design variables are defined in Fig. 11(a) and their values are listed in Table II. Although the cell contains a single slot, its two modes are coupled, so it already behaves as a second-order coupled-resonator filter and can be designed with the usual coupling-matrix approach [33]. The inter-mode coupling coefficient is extracted from the two pole frequencies,

$$k = \frac{f_2^2 - f_1^2}{f_2^2 + f_1^2}, \qquad (10)$$

and the external quality factor from the 3-dB bandwidth BW and the centre frequency f_0,

$$Q_e = \frac{2f_0}{\text{BW}}. \qquad (11)$$

Both quantities were mapped against the transition width and the clearances w and l by repeated full-wave simulation, and the dimensions were then chosen to realise a second-order response with $Q_e \approx 14.3$ and $k_{12} \approx 0.042$, i.e., $f_0 \approx 2.15$ GHz and BW ≈ 0.3 GHz (fractional bandwidth FBW $= \text{BW}/f_0 \approx 14\%$). A relatively large Q_e was used during tuning so that the even and odd resonances of the dual-mode cell remain clearly separated.

TABLE II. Dimensions of the proposed filters.

Symbol	Description	Value (mm)
a_{equ} (W)	Via-row spacing (centre to centre)	15
d	Via diameter	1
p	Via pitch	1.5
b	Fractal side length	12.5
g	Slot width	0.5
w	Fractal-to-via clearance	0.73
l	Fractal-to-edge clearance	1.12
–	Board size, one stage (without feeds)	17×17

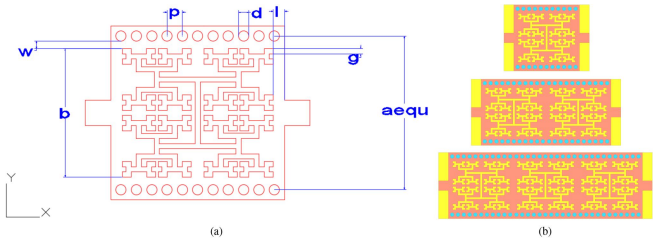


Fig. 11. (a) Design variables of the filters; (b) layouts of the one-, two- and three-stage filters.

B. Multi-Stage Filters

Higher-order filters are obtained by cascading identical third-iteration cells along the guide (Fig. 11(b)); the inter-cell coupling is controlled by the spacing between adjacent slots, and the dimensions were optimised in ADS in the same way as for the one-stage filter. The simulated responses are shown in Fig. 12. Both filters exhibit three reflection poles in the passband and a transmission zero on each side of it, which makes the skirts much steeper than in the one-stage case. Their centre frequency rises to about 2.3 GHz and their 3-dB bandwidth widens to about 0.5 GHz, because the electromagnetic interaction between neighbouring slots modifies the effective loading of each cell. The out-of-band rejection improves with the number of cells, at the expense of a longer board.

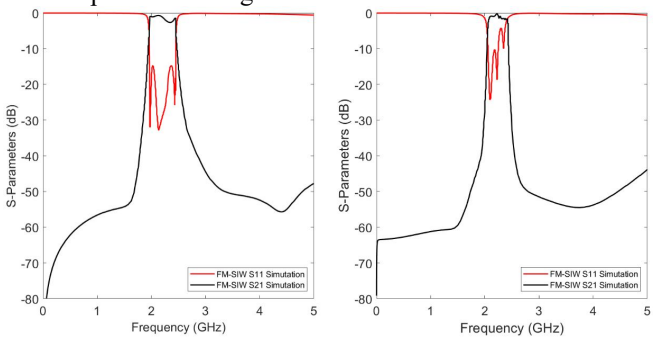


Fig. 12. Simulated *S*-parameters of the (a) two-stage and (b) three-stage filters.

C. Fabrication and Measurement

The one-stage filter was fabricated on 1.5-mm FR4 by CNC milling, with SMA connectors soldered to the feed lines, and was measured with a vector network analyser from 10 MHz to 6 GHz. Photographs of the prototype are shown in Fig. 13, and the measured and simulated responses are compared in Fig. 14.

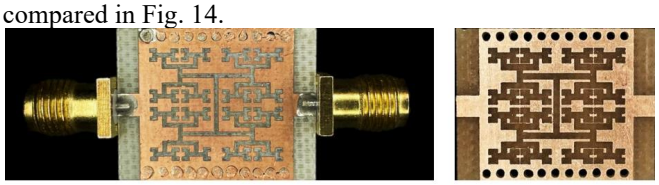


Fig. 13. Fabricated one-stage filter: (a) with SMA connectors; (b) close-up of the milled fractal slot.

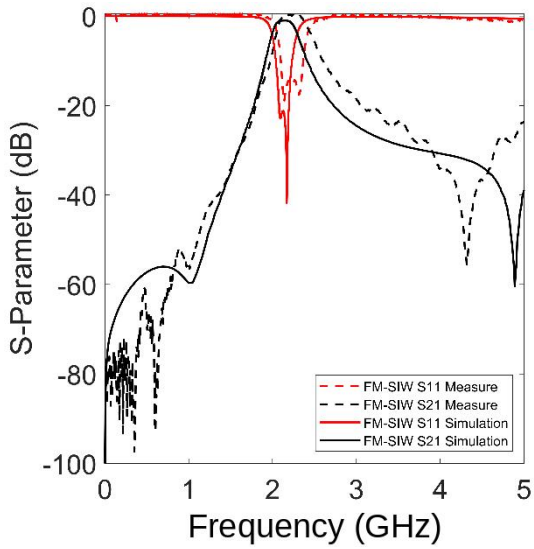


Fig. 14. Measured and simulated *S*-parameters of the one-stage filter.

The measured passband shows two poles, is centred at about 2.15 GHz, and has a 3-dB bandwidth of about 0.3 GHz. The minimum insertion loss is about 1.5 dB, including the two SMA connectors that are not part of the simulation, and the in-band return loss is about 19 dB. The rejection is about 45 dB in the lower stopband and about 30 dB in the upper stopband. The lower transmission zero is measured near 1 GHz, as predicted; the upper zero appears at about 4.3 GHz instead of the simulated 4.9 GHz. This shift, and the slight broadening of the passband, are attributed to the milling tolerance of the narrow slot segments, to the spread of the FR4 permittivity, and to the connector transitions.

The measured unwrapped phase of S_{21} is plotted in Fig. 15. It varies almost linearly across the passband, between about 1.9 and 2.15 GHz, which indicates a nearly flat group delay and low signal distortion.

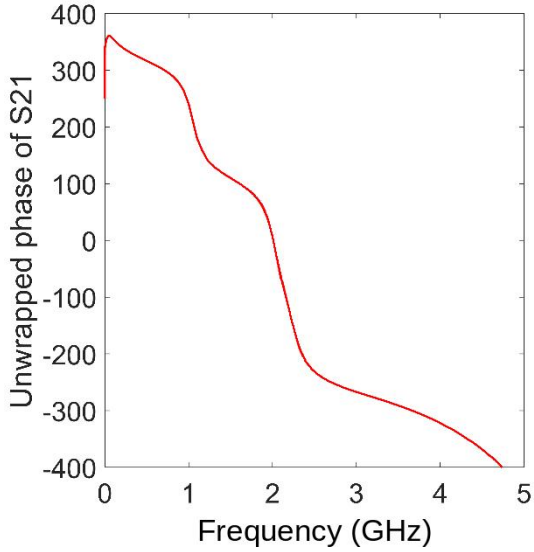


Fig. 15. Measured unwrapped phase of S_{21} of the one-stage filter.

VI. Discussion and Comparison

A. Loss Budget

An insertion loss of about 1.5 dB is reasonable for a narrow-band filter on FR4 but higher than that reported on low-loss laminates. The main contributions are the dielectric loss ($\tan\delta = 0.025$), the conductor loss along the long,

narrow fractal boundary, a small amount of radiation from the slot, and the two connectors. A substrate with $\tan\delta \approx 0.001$ would reduce the dielectric part by roughly an order of magnitude without changing the topology.

B. Comparison

Table III compares the proposed filter with related SIW fractal and metamaterial filters. Because the references operate at very different frequencies and on different substrates, the footprint is also given in units of λ_0^2, where $\lambda_0 = c_0/f_0$ is the free-space wavelength at the centre frequency. The proposed filter is more compact than the C-band fractal and hybrid designs, and it is the only one among them that combines an iteration study, constitutive-parameter retrieval and an equivalent circuit. The cross-fractal HMSIW filter of [27] is smaller in terms of λ_0^2 because it uses the half-mode cut and operates near 1.1 GHz; applying the half-mode cut to the present cell [31] reduces its width by a further factor of about two. The price paid for the low-cost FR4 substrate is a higher insertion loss than designs on low-loss laminates.

TABLE III. Comparison with related SIW fractal and metamaterial bandpass filters.

Ref.	Technique	f_0 (GHz)	IL/RL (dB)	FBW (%)	Size (λ_0^2)
[28]	H-shaped fractal slots, SIW	5.3	0.75/23	12.5	0.019
[27]	Cross-shaped fractal, HMSIW	1.13	0.8/11.8	4.3	0.004
[30]	Hybrid fractal + CSRR + DGS, HMSIW	5.2	1.1/14.5	26.3	0.061
This work	I–H fractal slot, SIW	2.15	1.5/19	14	0.015

VII. Conclusion

A space-filling I–H slot etched on the broad wall of an SIW has been shown to open a usable passband deep inside the evanescent band of the guide. Increasing the slot order within the same area lowers the passband from about 4.1 GHz to 2.15 GHz, which is roughly 59% below the cutoff of the unloaded waveguide. The extracted constitutive parameters and the dispersion curves reveal a backward-wave band immediately followed by a forward-wave band, and a compact lumped-element model reproduces the lower transmission zero and both resonant modes while linking each of them to a physical dimension. The measured single-cell filter on FR4 provides about 1.5 dB insertion loss, about 19 dB return loss, an almost linear in-band phase and a footprint of $0.12\lambda_0 \times 0.12\lambda_0$; cascading two or three cells sharpens the skirts considerably. Low-loss laminates and electronically tunable slot loadings will be investigated next.

References

[1] M. Bozzi, A. Georgiadis, and K. Wu. Review of substrate-integrated waveguide circuits and antennas. *IET Microwaves, Antennas & Propagation*, 5(8):909–920, 2011.

[2] D. Deslandes and K. Wu. Accurate modeling, wave mechanisms, and design considerations of a substrate integrated waveguide. *IEEE Transactions on Microwave Theory and Techniques*, 54(6):2516–2526, 2006.

[3] A. Iqbal, J. J. Tiang, S. K. Wong, M. Alibakhshikenari, F. Falcone, and E. Limiti. Miniaturization trends in substrate integrated waveguide (SIW) filters: A review. *IEEE Access*, 8:223287–223305, 2020.

[4] W. Che, C. Li, D. Zhang, and Y. L. Chow. Investigations on propagation and the band broadening effect of ridged rectangular waveguide integrated in a multilayer dielectric substrate. *IET Microwaves, Antennas & Propagation*, 4(6):674–684, 2010.

[5] R. Kumar and S. N. Singh. Design and analysis of ridge substrate integrated waveguide bandpass filter with octagonal complementary split ring resonator for suppression of higher order harmonics. *Progress In Electromagnetics Research C*, 89:87–99, 2019.

[6] Q. Lai, C. Fumeaux, W. Hong, and R. Vahldieck. Characterization of the propagation properties of the half-mode substrate integrated waveguide. *IEEE Transactions on Microwave Theory and Techniques*, 57(8):1996–2004, 2009.

[7] Y. Wang, W. Hong, Y. Dong, B. Liu, H. Tang, J. Chen, X. Yin, and K. Wu. Half mode substrate integrated waveguide (HMSIW) bandpass filter. *IEEE Microwave and Wireless Components Letters*, 17(4):265–267, 2007.

[8] X. L. Huang, L. Zhou, M. Völkel, A. Hagelauer, J. F. Mao, and R. Weigel. Design of a novel quarter-mode substrate-integrated waveguide filter with multiple transmission zeros and higher mode suppressions. *IEEE Transactions on Microwave Theory and Techniques*, 66(12):5573–5584, 2018.

[9] R. Asgharivaskasi, V. Mashayekhi, N. Azadi-Tinat, and M. Koohestani. Ultra-compact quad-band half-mode SIW bandpass filter for sub-6 GHz 5G applications. *Scientific Reports*, 15:30077, 2025.

[10] R. Moro, S. Moscato, M. Bozzi, and L. Perregrini. Substrate integrated folded waveguide filter with out-of-band rejection controlled by resonant-mode suppression. *IEEE Microwave and Wireless Components Letters*, 25(4):214–216, 2015.

[11] A. Parameswaran, P. Athira, and S. Raghavan. Miniaturizing SIW filters with slow wave technique. *AEU – International Journal of Electronics and Communications*, 84:360–365, 2018.

[12] D. F. Guan, P. You, Q. Zhang, Z. B. Yang, H. Liu, and S. W. Yong. Slow-wave half-mode substrate integrated waveguide using spoof surface plasmon polariton structure. *IEEE Transactions on Microwave Theory and Techniques*, 66(6):2946–2952, 2018.

[13] V. G. Veselago. The electrodynamics of substances with simultaneously negative values of ε and μ. *Soviet Physics Uspekhi*, 10(4):509–514, 1968.

[14] I. Gil, J. Bonache, J. García-García, F. Falcone, and F. Martín. Metamaterials in microstrip technology for filter applications. In *IEEE Antennas and Propagation Society International Symposium*, volume 1A, pages 668–671, 2005.

[15] R. Marqués, J. Martel, F. Mesa, and F. Medina. Left-handed-media simulation and transmission of EM waves in subwavelength split-ring-resonator-loaded metallic waveguides. *Physical Review Letters*, 89(18):183901, 2002.

[16] F. Falcone, T. Lopetegi, M. A. G. Laso, J. D. Baena, J. Bonache, M. Beruete, R. Marqués, F. Martín, and M. Sorolla. Babinet principle applied to the design of metasurfaces and metamaterials. *Physical Review Letters*, 93(19):197401, 2004.

[17] F. Falcone, T. Lopetegi, J. D. Baena, R. Marqués, F. Martín, and M. Sorolla. Effective negative-ε stopband microstrip lines based on complementary split ring resonators. *IEEE Microwave and Wireless Components Letters*, 14(6):280–282, 2004.

[18] Y. D. Dong, T. Yang, and T. Itoh. Substrate integrated waveguide loaded by complementary split-ring resonators and its applications to miniaturized waveguide filters. *IEEE Transactions on Microwave Theory and Techniques*, 57(9):2211–2223, 2009.

[19] X. C. Zhang, Z. Y. Yu, and J. Xu. Novel band-pass substrate integrated waveguide (SIW) filter based on complementary split ring resonators (CSRRs). *Progress In Electromagnetics Research*, 72:39–46, 2007.

[20] W. Che, C. Li, K. Deng, and L. Yang. A novel bandpass filter based on complementary split rings resonators and substrate integrated waveguide. *Microwave and Optical Technology Letters*, 50(3), 2008.

[21] S. S. Karthikeyan and R. S. Kshetrimayum. Harmonic suppression of parallel coupled microstrip line bandpass filter using CSRR. *Progress In Electromagnetics Research Letters*, 7:193–201, 2009.

[22] Y. Dong and T. Itoh. Miniaturized substrate integrated waveguide slot antennas based on negative order resonance. *IEEE Transactions on Antennas and Propagation*, 58(12):3856–3864, 2010.

[23] Y. Dong and T. Itoh. Composite right/left-handed substrate integrated waveguide and half mode substrate integrated waveguide leaky-wave structures. *IEEE Transactions on Antennas and Propagation*, 59(3):767–775, 2011.

[24] M. Danaeian, K. Afrooz, and A. Hakimi. Miniaturization of substrate integrated waveguide filters using novel compact metamaterial unit-

cells based on SIR technique. *AEU – International Journal of Electronics and Communications*, 84:62–73, 2018.

[25] G. Peano. Sur une courbe, qui remplit toute une aire plane. *Mathematische Annalen*, 36(1):157–160, 1890.

[26] J. Romeu and Y. Rahmat-Samii. Fractal FSS: A novel dual-band frequency selective surface. *IEEE Transactions on Antennas and Propagation*, 48(7):1097–1105, 2000.

[27] V. Sekar and K. Entesari. Miniaturized half-mode substrate integrated waveguide bandpass filters using cross-shaped fractals. In *IEEE 12th Annual Wireless and Microwave Technology Conference (WAMICON)*, pages 1–4, Clearwater Beach, FL, USA, 2011.

[28] A. M. Hamzah, L. Audah, and N. Alkhafaji. H-shaped fractal slots based highly miniaturized substrate integrated waveguide metamaterial bandpass filters for C-band applications. *Progress In Electromagnetics Research B*, 86:139–158, 2020.

[29] N. Muchhal, A. Chakraborty, K. Vishnoi, and S. Srivastava. Miniaturized and selective half-mode substrate integrated waveguide bandpass filter using Hilbert fractal for sub-6 GHz 5G applications. *IETE Journal of Research*, 69(10), 2023. doi: 10.1080/03772063.2021.2021816.

[30] N. Muchhal, M. Elkhouly, R. Z. Vintimilla, A. Chakraborty, and S. Srivastava. Design of hybrid fractal integrated half mode SIW band pass filter with CSRR and Minkowski defected ground structure for sub-6 GHz 5G applications. *Photonics*, 9(12):898, 2022.

[31] R. M. Hadi. Miniaturized bandpass filter using the metamaterial half-mode technique for substrate integrated waveguide. *International Journal of Computer Science Engineering Techniques*, 10(5):281–286, 2026.

[32] D. R. Smith, D. C. Vier, T. Koschny, and C. M. Soukoulis. Electromagnetic parameter retrieval from inhomogeneous metamaterials. *Physical Review E*, 71(3):036617, 2005.

[33] J.-S. Hong and M. J. Lancaster. *Microstrip Filters for RF/Microwave Applications*. John Wiley & Sons, New York, 2001.